Band Gap Engineering of a MoS_2 Monolayer through Oxygen Alloying: an *Ab-Initio* Study

N.F. Andriambelaza[a,*], R.E. Mapasha[a], N. Chetty[a,b]

[a] *Department of Physics, University of Pretoria, Pretoria 0002, South Africa*
[b] *National Institute for Theoretical Physics, Johannesburg, 2000, South Africa*

Abstract

Oxygen (O) alloying in a MoS_2 monolayer appearing in different shapes: line-ordered, cluster and random have been theoretically designed, for band gap engineering in order to extend its nanotechnological applications. The thermodynamic stability, structural and electronic properties of these alloy configurations at each concentration have been comparatively studied using the density functional theory methods. Based on the formation energy analysis, the O line-ordered alloys are most stable compared to the well known random and cluster alloys at high concentration, while at low concentration they compete. The lattice constants of all the alloyed systems decrease linearly with the increase in O concentration, consistent with Vegard's law. The Mo-O bond lengths are shorter than the Mo-S leading to a reduction in the band gap, based on density of state analysis. The partial charge density reconciling with the partial density of states analysis reveals that the band gap reduction is mainly contributed by the Mo $4d$ and O $2p$ orbitals as shown at the band edges of the density of states plots. Creation of stacking

of MoS_2 with MoO_2 gives metallic character, with Mo $4d$ orbital crossing the Fermi level. The O alloys in a MoS_2 monolayer should be considered to be an effective way to engineer the band gap for designing new nanoelectronic devices with novel performance.

Keywords: 2D materials, density functional theory, transition metal dichalcogenides, transition metal oxides, alloying.

---

1. Introduction

Since the emergence of nanotechnology, an advancement of electronic devices has continued unabated, in particular on the speed and size (reduction from three dimension (3D) to two dimension(2D)). In the last decade, 2D hexagonal materials emerged to be promising materials for the design of nanoelectronic devices due to their unique properties. The high charge carrier mobility, mechanical flexibility and strength reduced dimensionality, transparency, etc [1, 2, 3, 4] mostly measured on graphene [5], hexagonal boron nitride (h-BN) [6], transition metal dichalcogenides (TMD) [1, 7] can be mentioned. The recently synthesized 2D hexagonal-like TMD materials such as MoS_2, $MoSe_2$, $MoTe_2$, WS_2, WSe_2, WTe_2 and CrS_2 [1, 7, 8] are particularly interesting due to their robust mechanical character and relatively large band gap [9, 10]. Recently, the hexagonal-like transition metal oxides (TMO) materials such as MoO_2, WO_2 and CrO_2 monolayers were predicted using density functional theory (DFT) and found to be semiconductors with the band gaps of 0.97 eV, 1.37 eV and 0.5 eV respectively [9, 10]. To examine the stability of these oxide based nanomaterials, Ataca *et al.* [9] performed a phonon calculation and no imaginary vibration frequencies were noted sug-

gesting mechanical stability.

Although the pristine TMD and TMO monolayers inherently possess the exotic physical properties [9, 10, 11], tuning their band gaps continuously is essential for designing nanoelectronics devices. Diverse methods such as alloying [12, 13, 14, 15], creation of point defects [16, 17, 18, 19], doping [20, 21, 22, 23, 24], application of an axial strain [25, 26, 27, 28, 29] etc. efficiently engineer the band gap of a TMD material. Alloying in a MoS_2 monolayer has been widely studied experimentally using chemical vapor deposition (CVD) methods [30, 31], and theoretically using density functional theory (DFT) methods [12, 14, 15, 32, 33]. Alloys can appear in different popular ground state configurations such as random, cluster, lines, triplets (form a triangle-like) etc. [34]. Experimental studies of the tungsten (W) alloys at the molybdenum (Mo) sites revealed that random distribution occurs spontaneously at about 1030°C [30, 31]. Photoluminescence experiments revealed that the band gap of the MoS_2 monolayer is fine tuned with the variation of the W concentration. Furthermore, DFT studies revealed that the hybridization of the d orbitals of the W atoms with those of Mo atoms at the vicinity of the band edges is mainly responsible for the increase of the band gap [35, 31]. Very recently, Andriambelaza *et al.* [14] performed a comparative study of chromium (Cr) line-ordered alloys with the random distribution alloys at the Mo sites of a MoS_2 monolayer using the DFT method. It was found that the line-ordered alloys are energetically favorable compared to the random alloys. Both distributions fine tune the band gap with the same magnitudes (1.65 eV to 0.86 eV).

For the sulfur (S) sites, the selenium (Se) and tellurium (Te) alloys are

popular studied and their experimental characterizations [36, 37] revealed the spontaneous random distribution at high temperatures. However, the DFT calculations (at zero Kelvin) indicated the ordered phase to be preferable as compared to the random distribution [8, 36]. Our previous DFT study revealed that the Te line-ordered alloys compete very well with the random alloys in terms of stability [38]. Furthermore, the band gap of the MoS_2 monolayer is fine tuned within a range that can be useful for designing novel nanotechnological devices [15, 36].

Oxygen (O) alloys in a MoS_2 monolayer have not yet been explored, although it belongs to the same group as S, Se, and Te atoms on the periodic table. Moreover, a hexagonal MoO_2 monolayer has been predicted to be isostructural to the MoS_2, $MoSe_2$ and $MoTe_2$ monolayers [9, 10]. Generally, the Se and Te atoms have more atomic radii than the S atoms, whereas the O atom possesses the smallest. Therefore, a comprehensive study on the electronic and structural properties of O alloys is necessary to compare with those of Te and Se alloys.

In this paper, various O alloy configurations in the form of random, line-ordered and cluster distributions in a 5×5 supercell of a MoS_2 monolayer are studied. However, studying all the possible alloy configurations for each distribution at every concentration is intractable and computationally time consuming using the first-principle methods. At each alloy distribution and concentration, selected configurations were optimized. Since the random and cluster distributions are the most popular studied alloys and known to exist experimentally, we compare their results with those of the line-ordered alloys.

2. Computational details

DFT method implemented within the Vienna $Ab-initio$ Simulation Package (VASP) [39] is performed to study the electronic structure of the O alloys in a MoS_2 monolayer. To describe the exchange-correlation interaction, the Perdew-Burke-Ernzerhof (PBE) parametrization within the generalized gradient approximation (GGA) [40] is used. The flavor of GGA exchange correlation functional is known to underestimate the band gap value of semiconductor materials due to the absence of the derivative discontinuity feature and delocalized errors [41]. To overcome this issue, the hybrid functionals have been proposed [42]. In this paper, the screened hybrid functional of Heyd-Scuseria-Ernzerhof (HSE06) is used by mixing 25% (AEXX = 0.25) of the exact nonlocal Hartree-Fock (HF) exchange to the PBE exchange [41, 42]. The projector augmented wave (PAW) method is employed to define the core and valence electron interactions. An energy cut-off of 300 eV is chosen for the expansion of the wave functions in the plane wave basis. A supercell of 5×5 is chosen at each concentration to model the alloys and a k-point sampling of $3 \times 3 \times 1$ is suitable for this large supercell. Atomic positions and lattice vectors are fully relaxed during the calculations with a force and energy convergence threshold of 2×10^{-2} eV/Å and 10^{-5} eV respectively. To avoid periodical interaction along the vertical axis, a vacuum space of 20 Å is considered.

The stability of the various alloy configurations at each concentration confined between to the two pristine materials is defined by the formation energy:

$$E_{form} = E_{MoS_{(1-x)}O_x} - (1-x)E_{MoS_2} - xE_{MoO_2} \ , \tag{1}$$

where $E_{MoS_{(1-x)}O_x}$ is the total energy of the system at each x O concentration. E_{MoS_2} and E_{MoO_2} are the total energies of the pristine MoS_2 and MoO_2 monolayers, respectively.

To generate the random alloy configurations, the special quasirandom structure (SQS) is adopted. The O substitutional alloy in a MoS_2 monolayer can be written in a general form $A_{1-x}B_x$, where A and B correspond to the S and O atoms, respectively. Generally, the correlation functions of an ideal alloy are given by $\prod_{k,m}(ideal) = (2x-1)^k$ [33], where k=2, 3,... indicate the pair, triple correlation, etc. and m=1, 2, 3,... correspond to the first, second and third-nearest distance, etc. Previous studies reported that the alloy nearest-neighbor interaction greatly dominates the properties of host materials, whereas the effects of far away interaction are significantly small [33, 43, 44]. Therefore, only the nearest-neighbor pairs are considered in this study.

In the other side, the pair correlation function can be written as: $\prod_{2,1}(r) = \frac{1}{N_b}\sum_{j,k=1,N}^{j>k} i_j i_k$, where $i = +1$ if the site is occupied by A atom and $i = -1$ if the site is occupied by B atom. N_b and N are the total number of bonds and chalcogen sites in the supercell, respectively. Assume that the total number of pair neighboring bonds of A-A, A-B and B-B in the supercell are denoted by N_{AA}, N_{AB} and N_{BB}, respectively. They can be expressed as [14, 33]:

$$\begin{cases} (N_{AB} + 2N_{AA})/Z = N_A = N(1-x) \\ (N_{AB} + 2N_{BB})/Z = N_B = Nx \\ N_b = N_{AA} + N_{BB} + N_{AB} \end{cases} \tag{2}$$

N_A and N_B indicate the total number of sites occupied by A and B atoms in the supercell, respectively. Z denotes the coordination number of the chalcogen atoms in the lattice. Substituting Eqn. 2 into $\prod_{2,1}(r)$ and applying some algebra we get:

$$\Pi_{2,1}(r) = \frac{N_{AA} + N_{BB} - N_{AB}}{N_{AA} + N_{BB} + N_{AB}} = 1 - 4x + \frac{8N_{BB}}{Nz}. \quad (3)$$

This equation shows clearly that the correlation functions can be expressed in terms of the number of B-B bond (N_{BB}). The random alloy configurations at each concentration are modeled in such a way that the correlation functions are identical to the ideal alloys up to the nearest-neighbor pairs ($\prod_{2,1}(ideal) = \prod_{2,1}(r)$). It results that the number of B-B bond for the random configuration should be $N_{BB} = \frac{1}{2}x^2NZ$ [14, 33]. In this study, N is the total number of chalcogen atoms present in the 5 $\times$ 5 supercell (N=50).

3. Results and discussion

3.1. Pristine MoS_2 and MoO_2 monolayers

The structure of the TMD and TMO monolayers can be classified into two types: 2H and 1T [9]. Ataca *et al.* [9] have established that MoS_2 (TMD) and MoO_2 (TMO) monolayers are more stable in 2H structure. Top and side views of a 5 $\times$ 5 supercell of the MoS_2 and MoO_2 monolayers are shown in Fig. 1(a) and Fig 1(b), respectively. The hexagonal-like pattern of the 2H structure is clearly seen on the top view of the structures, where the Mo and S (O) atoms occupy different sublattices. From the side view, it can be seen that the 2D MoS_2 and MoO_2 are made by one layer of Mo

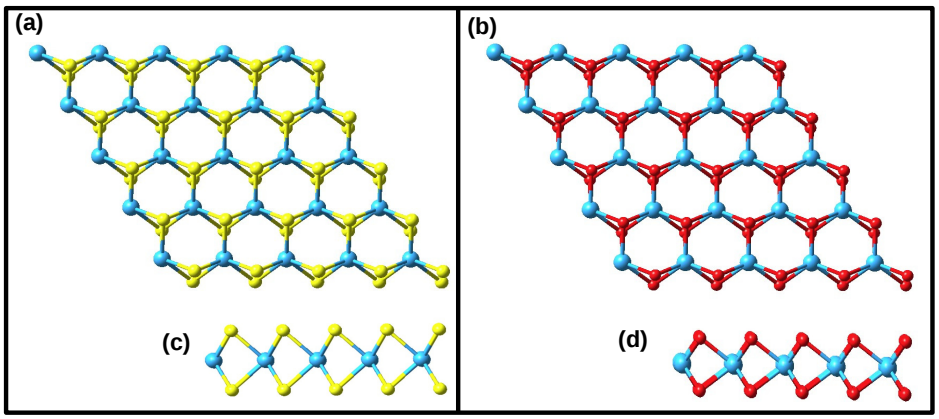

Figure 1: Top and side view of the ((a) and (c)) MoS_2 and ((b) and (d)) MoO_2 monolayers. The blue, red and yellow spheres indicate the Mo, O and S atoms respectively.

atom sandwiched in between two S (O) layers. To understand the nature of bonding between Mo atom and S (O) atom, Bader charge analysis was considered. It was found that the Mo atom has a depletion of 1.18 electron while each S atom accumulates 0.58 electron. This charge sharing reveals a covalent bond between Mo and S atoms [45]. This covalency is also confirmed by the electron localized function (ELF) analysis, where a non spherically symmetry of the regions with high ELF around S atoms and a tendency of the lobes towards the Mo are observed [46, 47].

To study the alloyed real material, the knowledge of the structural, energetics and electronic properties of the pristine host is essential. The structural and energetic properties of the MoS_2 and MoO_2 monolayers are listed in Table. 1. It was found that the HSE06 functional underestimates the lattice parameter while GGA functional overestimates it [52]. These results are in good agreement with the previous experimental and theoretical data as

Table 1: Lattice constant a(Å), bond length d[Mo-X (X = S, O)](Å), cohesive energy E_{coh} (eV/atom), formation energy E_{form} (eV), band gap values E_{gap} (eV) of the pristine MoS_2 and MoO_2 monolayers.

System	Method		a	d[Mo-X]	E_{coh}	E_{form}	E_{gap}
MoS_2	Previous work	Expt.	3.16[a,b]	2.41[i]	-	-	1.90[n]
		GGA	3.18[c], 3.20[g]	2.41[d], 2.408[h]	5.18[g]	-0.842[c]	1.652[e], 1.70[d]
		HSE06	3.153[h], 3.155[f]	2.391[h], 2.39[d]	-	-	2.10[d], 2.23[o]
	This work	GGA	3.18	2.41	6.54	-1.40	1.67
		HSE06	3.153	2.38	5.69	-1.47	2.17
MoO_2	Previous work	Expt.	-	-	-	-	-
		GGA	2.82[c], 2.83[l,j]	2.05[j,l]	7.55[k]	-1.73[c]	0.98[m], 0.97[d]
		HSE	-	-	-	-	1.48[l]
	This work	GGA	2.81	2.05	6.14	-2.25	0.97
		HSE06	2.79	2.02	5.77	-3.02	1.48

[a]ref. [48], [b]ref. [49], [c]ref. [10], [d]ref. [47], [e]ref. [50], [f]ref. [21], [g] ref. [51], [h]ref. [52], [i]ref. [53], [j]ref. [11], [k]ref. [9], [l]ref. [54], [m]ref. [55], [n]ref. [7], [o]ref. [56]

seen in Table. 1. The total density of states (TDOS) and partial density of states (PDOS) of the MoS_2 and MoO_2 monolayers are evaluated and plotted in Figs. 2(a-b). We found that these two pristine systems are band gap semiconductors. Quantitatively, the band gap values of 1.67 eV (2.17 eV) and 0.98 eV (1.48 eV) are measured using GGA (HSE) functional for the MoS_2 and MoO_2 monolayers, respectively. These values are in good agreement with previously reported data as presented in Table. 1. The PDOS

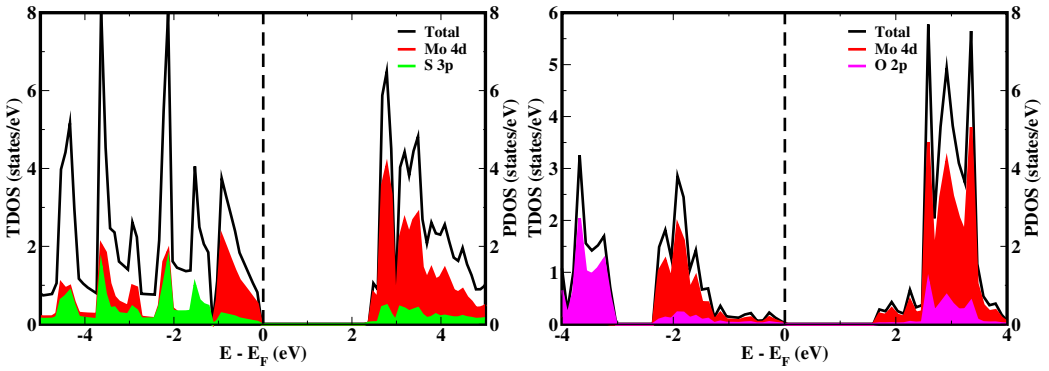

Figure 2: Total density of states (TDOS) and partial density of states (PDOS) of the (a) MoS_2 and (b) MoO_2 monolayers obtained using HSE06 functional. Black solid lines indicate the TDOS of the MoS_2 and MoO_2 monolayers. The red, green and magenta lines correspond to the d orbital of the Mo atom, the p orbitals of the S and O atoms, respectively. The dashed vertical lines represent the Fermi level.

plots clearly indicate that the conduction band minimum (CBM) states of both the MoS_2 and MoO_2 monolayers arise mainly from the Mo 4d orbitals. On the other hand, the valence band maximum (VBM) states of both systems are contributed by the hybridization of the Mo 4d orbitals and the S 3p (O 2p) orbitals. These orbital contributions are consistent with the results reported in Refs [11, 21].

3.2. Identification of the various O alloy configurations

Generally, the properties of an alloy material greatly depend on the structural arrangement and composition variation. In this section, various alloy configurations at different O concentrations are discussed. The identification of the O line-ordered alloy, typical O cluster, and various O random alloy configurations at each concentration is described. In fact, the vital question associated with this section is how to generate these various configurations

of O alloys?

To explain the O line-ordered alloy configurations studied in this work, Fig. 3 shows a schematic representation of labeled 5 × 5 supercell of a MoS_2 monolayer. For the formation of the O line-ordered alloys, S atoms are substituted with O atoms along the zigzag direction of the supercell. The labels u, b, r_1, r_2, r_3, r_4 and r_5 in the Fig. 3 are used to name the distinct configurations of O line-ordered alloys in a MoS_2 monolayer, obeying the periodic boundary conditions (PBC) to avoid the double counting. The letter u and b refer to the upper and the bottom layers of S atom respectively, sandwiching the Mo layer. The labels r_1, r_2, r_3, r_4 and r_5 indicate the first, second, third, fourth and fifth row of the S atoms in the 5 × 5 supercell, as clearly seen in Fig. 3. There are seven S concentrations (%) studied in this work: 0.0 (0%), 0.1 (10%), 0.3 (30%), 0.5 (50%), 0.7 (70%), 0.9 (90%) and 1.0 (100%). Several unique O line-ordered configurations at each concentration are identified and studied. Table. 2 lists all the identified O line-ordered alloy configurations. The 0.1 concentration of O atoms in a 5 × 5 supercell of a MoS_2 monolayer typically means five O atoms substitute five S atoms. For the continuous line-ordered alloy, one unique configuration is identifiable at this concentration, i.e the O atoms replacing the upper (u) S atoms in row 1 (r_1) can be denoted as O@r_{1u}. Obeying PBC, this configuration is the same as O$_@r_{2u}$, O$_@r_{3u}$, O$_@r_{1b}$, O$_@r_{2b}$, etc. Therefore, this configuration is uniquely called the line-ordered alloy configuration 1 at 0.1 concentration ($C_{1L(0.1)}$).

At 0.3 concentration, fifteen O atoms replace the S atoms in the system. Eight unique O line-ordered configurations (configuration $C_{1L(0.3)}$ to $C_{8L(0.3)}$) are also identified from Fig. 3 and enumerated in Table. 2. Their representa-

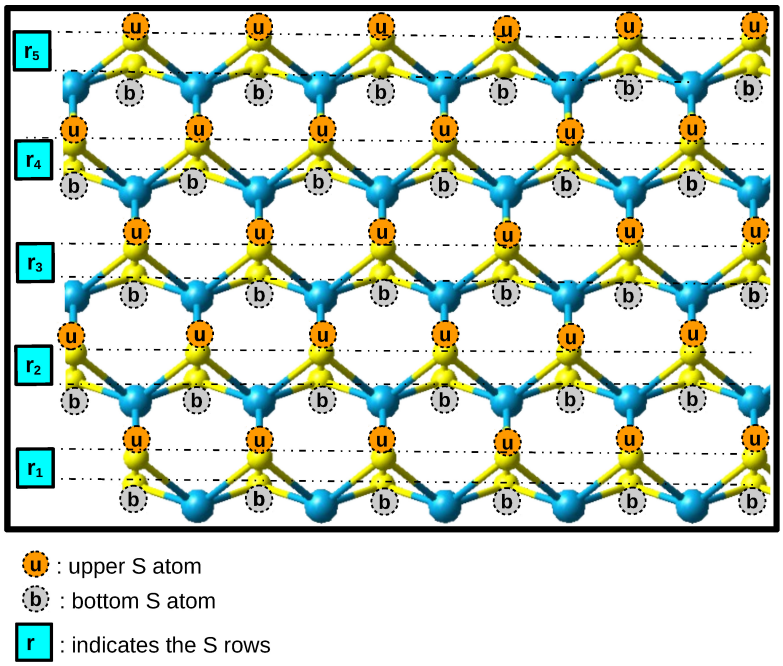

Figure 3: A schematic representation of a MoS_2 monolayer used to identify the line ordered alloys at every concentration. The diagram shows the three different layers of atoms. The blue and yellow spheres represent the Mo and S atoms, respectively. The labels u and b depict the upper and bottom S atoms. The label r indicates the rows.

tions are formulated the same way as that of 0.1 concentration. For instance, $C_{1L(0.3)}$ is the first line-ordered alloy configuration at 0.3 concentration. It is constituted by line of O atoms occupying row 1 (r_1) on the upper (u) layer and two rows r_1 and r_3 on the bottom (b) layer. It is denoted as $O_{@}r_{1ub}r_{3b}$ as seen in Table. 2. The same description is applicable to all the possible O line-ordered alloys at this concentration (see Table. 2). At 0.5 concentration, the number of the S and O atoms are the same (25 S atoms and 25 O atoms). Following the same pattern as in 0.1 and 0.3 concentrations, the permutation of the O rows gives sixteen unique line-ordered alloy configurations named as configuration $C_{1L(0.5)}$ to $C_{16L(0.5)}$. At 0.5 concentration, there is a special configuration where the O atoms fully cover the top layer and the S atoms

Table 2: All the possible line-ordered alloy configurations identified in a 5 × 5 supercell of MoS_2 monolayer at different concentrations. The thermodynamic stability of these various configurations will be checked. The labels u and b correspond to the upper and bottom S atoms. The letter r indicates the number of rows and the letter C stands for configuration.

	Concentration				
Conf.	0.1	0.3	0.5	0.7	0.9
C_{1L}	$O@r_{1u}$	$O@r_{1ub}r_{3b}$	$O@r_{1ub}r_{2u}r_{3u}r_{4u}$	$O@r_{2ub}r_{3u}r_{4ub}r_{5ub}$	$O@r_{1u}r_{2ub}r_{3ub}r_{4ub}r_{5ub}$
C_{2L}	-	$O@r_{1ub}r_{2u}$	$O@r_{1ub}r_{2ub}r_{3u}$	$O@r_{1u}r_{2u}r_{3u}r_{4ub}r_{5ub}$	-
C_{3L}	-	$O@r_{1u}r_{2u}r_{3u}$	$O@r_{1ub}r_{2u}r_{3ub}$	$O@r_{1b}r_{2u}r_{3u}r_{4ub}r_{5ub}$	-
C_{4L}	-	$O@r_{1u}r_{2u}r_{3b}$	$O@r_{1u}r_{2u}r_{3u}r_{4u}r_{5u}$	$O@r_{2u}r_{3ub}r_{4ub}r_{5ub}$	-
C_{5L}	-	$O@r_{1u}r_{2u}r_{4u}$	$O@r_{1u}r_{2u}r_{3u}r_{4u}r_{5b}$	$O@r_{1ub}r_{2u}r_{3u}r_{4ub}r_{5u}$	-
C_{6L}	-	$O@r_{1u}r_{2u}r_{4b}$	$O@r_{1u}r_{2u}r_{3u}r_{4b}r_{5b}$	$O@r_{1b}r_{2b}r_{3ub}r_{4u}r_{5ub}$	-
C_{7L}	-	$O@r_{1u}r_{2b}r_{3u}$	$O@r_{1b}r_{2u}r_{3b}r_{4u}r_{5b}$	$O@r_{1b}r_{2u}r_{3b}r_{4ub}r_{5ub}$	-
C_{8L}	-	$O@r_{1u}r_{2b}r_{4u}$	$O@r_{1ub}r_{2ub}r_{4u}$	$O@r_{1ub}r_{2b}r_{3ub}r_{4u}r_{5b}$	-
C_{9L}	-	-	$O@r_{1ub}r_{2u}r_{3u}r_{4b}$	-	-
C_{10L}	-	-	$O@r_{1ub}r_{2u}r_{3u}r_{5u}$	-	-
C_{11L}	-	-	$O@r_{1ub}r_{2u}r_{3u}r_{5b}$	-	-
C_{12L}	-	-	$O@r_{1ub}r_{2b}r_{3u}r_{5b}$	-	-
C_{13L}	-	-	$O@r_{1ub}r_{2u}r_{3b}r_{5b}$	-	-
C_{14L}	-	-	$O@r_{1ub}r_{2b}r_{3u}r_{4u}$	-	-
C_{15L}	-	-	$O@r_{1ub}r_{2u}r_{3b}r_{4u}$	-	-
C_{16L}	-	-	$O@r_{1ub}r_{2b}r_{4ub}$	-	-

fully cover the bottom layer. This configuration is known as *Janus* TMD structure [57]. It has been synthesized for the study of Se atoms in a MoS_2 monolayer. To generate the various O line-ordered alloy configurations at 0.7 concentration, we take all the configurations identified at 0.3 concentration

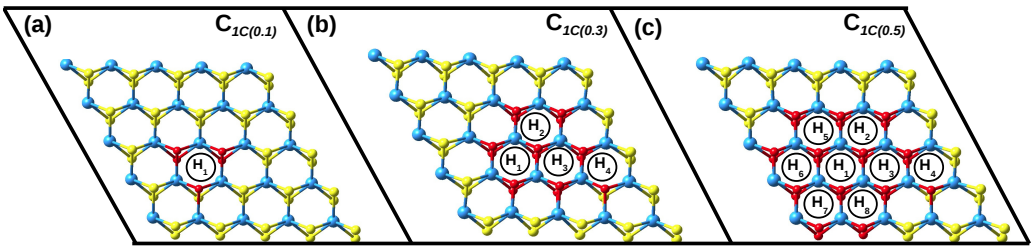

Figure 4: The geometric structures of the O atoms clustered in a MoS_2 monolayer viewed from the top at 10%, 30% and 50% concentrations. The blue, red and yellow spheres indicate the Mo, O and S atoms respectively.

and exchange the O with S atoms. Ditto to 0.9 concentrations.

The O cluster alloy configurations are also considered in this study. Basically, an O cluster configuration is constructed in such a way that all the O atoms are grouped together. Figs. 4(a-c) show typical cluster configurations at 0.1, 0.3 and 0.5 concentrations, respectively. At 0.1 concentration, the five O atoms occupy one hexagonal ring-like, denoted as H_1 indicated in Fig. 4(a). Three of the O atoms occupy all the three S sites of the upper layer (u) and form a triangle-like configuration, whereas the remaining two occupy the bottom layer (b). This cluster configuration is called $C_{1C(0.1)}$ in this work. At 0.3 concentration, the fifteen O atoms are grouped in the middle of the 5×5 supercell of a MoS_2 monolayer replacing the S atoms obeying the PBC. In this configuration, the fourteen O atoms occupy the hexagons H_1, H_2 and H_3 with one extra O atom overlapping to H_4 as shown in Fig. 4(b), and this configuration is denoted as $C_{1C(0.3)}$. The last cluster configuration presented in Fig. 4(c) corresponds to the 0.5 concentration. The O atoms are grouped together covering seven hexagons H_1, H_2, H_3, H_5, H_6, H_7 and

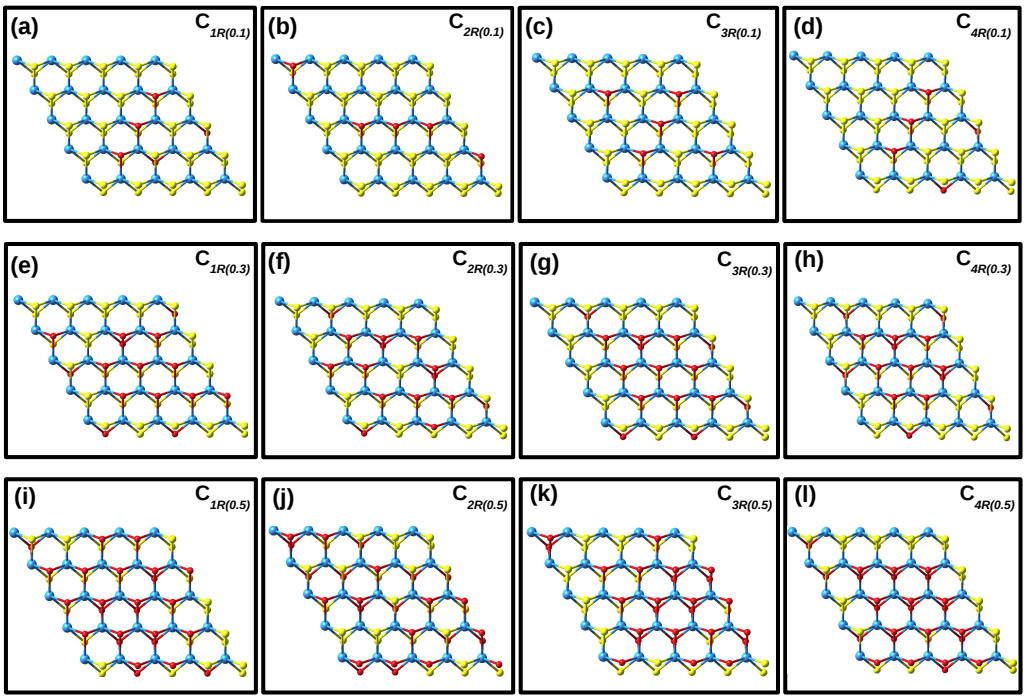

Figure 5: The selected geometric structures of the various O random alloy configurations in a MoS_2 monolayer viewed from the top at 10% (a-d), 30% (e-h) and 50% (i-l) concentrations. The blue, red and yellow spheres indicate the Mo, O and S atoms respectively.

H_8 in Fig. 4(c). One O atom is overlapping in H_4 as noted in Fig. 4(c). This cluster configuration at 0.5 concentration is called configuration $C_{1C(0.5)}$.

The last O alloy shape that we are considering in this paper is the most popular random distribution alloy. The challenge in the random alloy is the possibility of multiple configurations at each concentration. In this study, the special quasi-random structure (SQS) method proposed by Zunger et al. [58] is used to generate the various O random alloy configurations. The

SQS algorithm described in the Refs. [14, 33] which mimics an infinite perfect random alloy based on the behavior of the first nearest-neighbor atoms has been considered in this study. Obeying this method, the number of required alloy nearest-neighbor bonds are 2, 16 and 44 for 0.1, 0.3 and 0.5 concentrations respectively in a 5×5 supercell. At each concentration, many possible configurations can be formed. Considering a high computational cost, only selected alloy configurations that are spontaneously occur experimentally are shown in Fig. 5 are optimized. These special configurations are denoted as configuration $C_{1R(0.1)}$, $C_{2R(0.1)}$, $C_{3R(0.1)}$ and $C_{4R(0.1)}$ for 0.1 concentration, configuration $C_{1R(0.3)}$, $C_{2R(0.3)}$, $C_{3R(0.3)}$ and $C_{4R(0.3)}$ for 0.3 concentration, and configuration $C_{1R(0.5)}$, $C_{2R(0.5)}$, $C_{3R(0.5)}$ and $C_{4R(0.5)}$ for 0.5 concentration as presented in Fig. 5.

In the next section, the comparative studies of random, cluster and line-ordered alloy configurations at different concentrations are considered.

3.3. Thermodynamic stabilities of the MoS_2 monolayer alloyed with O atoms

As a common practice, in $ab-initio$ studies the relative thermodynamic stability of any alloy configuration is usually evaluated using the formation energy analysis defined in Eqn. 1.

In this study, the calculated formation energy values of all alloy configurations considered are summarized in Table. 3. The bold energy values represent the most energetically stable configuration for each type of alloy at every concentration. As seen in Table. 3, the formation energy values are positive, but with the small magnitude of the order 10^{-2} eV. The DFT calculations performed at static conditions may contribute to these positive

Table 3: Formation energy in meV values of various unique O line-ordered, random and cluster alloy configurations at 0.1, 0.3, 0.5, 0.7 and 0.9 concentrations. The letter C stands for configuration and the subscripts L, R and C indicate the line-ordered, random and cluster alloy configurations respectively. The bold values indicate the most energetically stable configuration for each type of alloy at every concentration.

		Concentration				
Type	Conf.	0.1	0.3	0.5	0.7	0.9
Line	C_{1L}	**31.12**	57.13	62.57	46.74	**15.89**
	C_{2L}	-	55.81	60.84	57.82	-
	C_{3L}	-	73.59	58.87	42.75	-
	C_{4L}	-	56.54	101.68	47.11	-
	C_{5L}	-	76.88	76.64	59.71	-
	C_{6L}	-	**52.87**	**53.90**	**39.32**	-
	C_{7L}	-	62.73	65.40	48.60	-
	C_{8L}	-	59.82	59.98	44.76	-
	C_{9L}	-	-	57.54	-	-
	C_{10L}	-	-	76.95	-	-
	C_{11L}	-	-	55.28	-	-
	C_{12L}	-	-	60.89	-	-
	C_{13L}	-	-	61.82	-	-
	C_{14L}	-	-	58.11	-	-
	C_{15L}	-	-	64.28	-	-
	C_{16L}	-	-	57.92	-	-
Random	C_{1R}	29.96	59.62	68.20	46.20	15.02
	C_{2R}	30.23	59.08	60.98	43.01	17.06
	C_{3R}	30.06	58.48	64.55	41.81	16.40
	C_{4R}	**29.59**	**56.77**	**59.98**	**39.28**	**14.74**
Cluster	C_{1C}	**27.91**	**54.61**	**58.78**	**42.46**	**15.80**

formation energy values. Therefore, the small positive values should not hinder the possibility of synthesizing a MoS_2 monolayer alloyed with O atoms.

The top part of Table. 3 summarizes the formation energy of the various O line-ordered alloy configurations defined in Table 2. Amongst of them, the configurations $C_{1L(0.1)}$, $C_{6L(0.3)}$, $C_{6L(0.5)}$, $C_{6L(0.7)}$ and $C_{1L(0.9)}$ are found to be energetically stable at 0.1, 0.3, 0.5, 0.7 and 0.9 concentrations respectively. The corresponding atomic structures of the configurations $C_{1L(0.1)}$, $C_{6L(0.3)}$ and $C_{6L(0.5)}$ are depicted in Figs. 6(a-c). Those of configurations $C_{6L(0.7)}$ and $C_{1L(0.9)}$ are simply the inverses of the configurations $C_{6L(0.3)}$ and $C_{1L(0.1)}$ respectively, i.e formed by exchanging the S and O atoms in the supercell system. We observe in Table. 3 and Fig. 7 that the configuration $C_{1L(0.1)}$ is more stable followed by $C_{1L(0.9)}$, $C_{6L(0.3)}$, $C_{6L(0.7)}$ and $C_{6L(0.5)}$, indicating that the formation energies of O alloys are concentration dependent as shown by the parabolic curve. This trend is in agreement with the previous studies of well known random and cluster alloys [33, 35].

Just like in some ideal alloys [14, 13, 32, 33], our 50/50 concentration alloy is the most energetically unfavorable. However, this observation contradicts that of Te alloy in a MoS_2 monolayer where 0.7 concentration is the least in stability [12, 15, 38]. At this concentration, the most stable configuration is configuration $C_{6L(0.5)}$ and can be defined as $O_{@}r_{1u}r_{2u}r_{3u}r_{4b}r_{5b}$, while the most unstable one is configuration $C_{10L(0.5)}$ given by $O_{@}r_{1u}r_{2u}r_{3u}r_{4u}r_{5u}$. This latter clearly shows that all five O rows are found in the upper layer and S atoms on the bottom layer or vice versa considering the translation symmetry operation. In addition, the O atoms fully cover the upper layer of S atoms. This typical structural arrangement has been discovered in the case of a

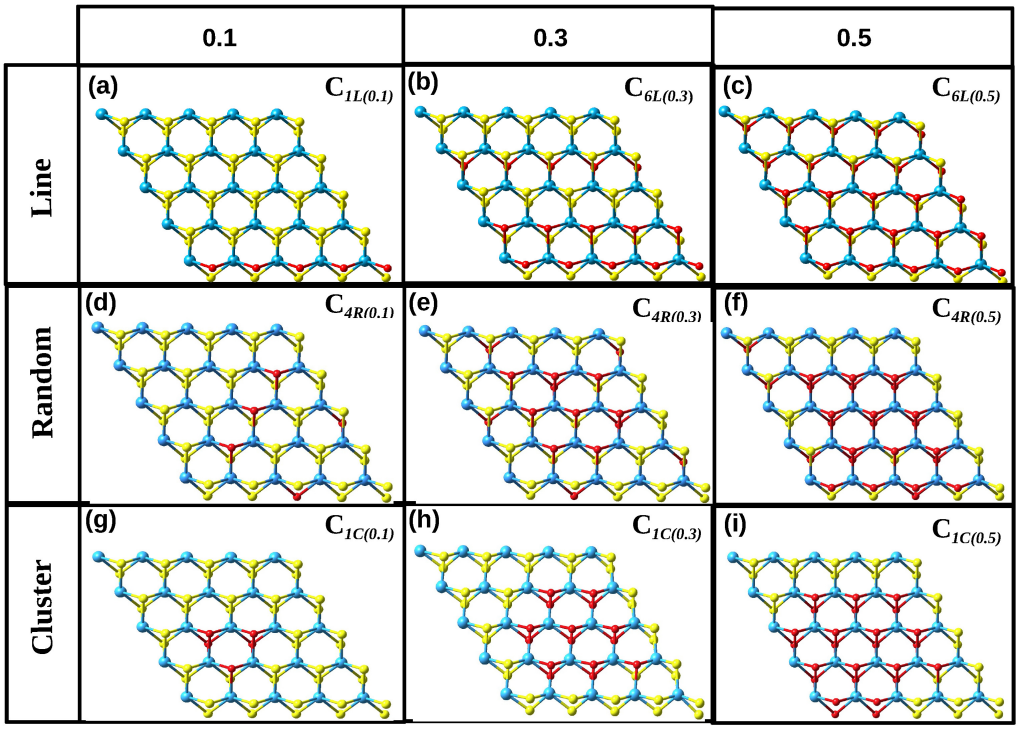

Figure 6: The optimized structures of the most energetically stable configuration at 0.1, 0.3 and 0.5 concentrations for line-ordered (a-c), random (d-f) and cluster (g-i) alloys. The blue, red and yellow spheres indicate the Mo, O and S atoms respectively.

MoS_2 monolayer alloyed with Se and Te atoms [12, 38, 59]. Also, it has been experimentally synthesized at high temperatures [57]. A common aspect with 0.5 concentration has been found at 0.3 concentration. The most stable configuration at 0.3 concentration is $C_{6L(0.3)}$ given by $O_{@}r_{1u}r_{2u}r_{4b}$ and the most unstable one is $C_{4L(0.3)}$ given by $O_{@}r_{1u}r_{2u}r_{3u}$. We observe that for each layer the lines of O atom prefer to be adjacent to each other but for

the different layer, they do not prefer to be superjacent to each other (see Fig.6(b) and Fig.6(c)). These observations and the diversity of the formation energy values summarized in Table. 3 reveal that the formation energy of the O alloy in a MoS_2 monolayer is governed by the concentration as well as the atomic arrangement.

The middle part of Table. 3 shows the formation energy of the selected random alloy configurations defined in the previous section. Amongst of them, the configurations $C_{4R(0.1)}$, $C_{4R(0.3)}$, $C_{4R(0.5)}$, $C_{4R(0.7)}$ and $C_{4R(0.9)}$ have the lowest formation energies at $0.1, 0.3, 0.5, 0.7$, and 0.9 concentration respectively. From Fig. 5 and Table. 3, we realize that the stability of the O random alloys depends on the distribution of the O atoms in the upper and bottom layer of the supercell. For the configuration to be most energetically favorable, the number of O atom in the upper and bottom layers must be close. For instance, at 0.3 concentration, configurations $C_{1R(0.3)}$, $C_{2R(0.3)}$, $C_{3R(0.3)}$ and $C_{4R(0.3)}$ have 10, 10, 9 and 8 O atoms in the upper layer and 5, 5, 6 and 7 O atoms in the bottom layer, respectively. According to Table. 3, configuration $C_{4R(0.3)}$ is most stable. That is, the larger the difference between the number of O atom in the upper and bottom layers, the more the random alloy system unstable. The similar trend is noted in other concentrations. However, the difference in formation energy values is relatively very small between the various configurations of the same concentration (less than 0.02 eV). This suggests that these configurations might co-exist at finite temperature.

Fig. 7 compares the formation energies of the lowest energy configurations at each concentration for the different alloy shapes. This gives an insight for

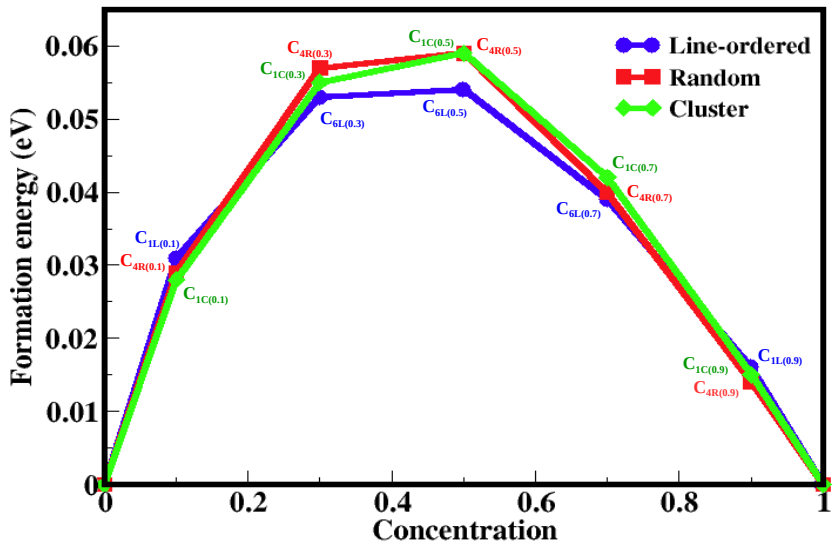

Figure 7: Variation of the formation energies with respect to the O concentration for the lowest energy configuration of the O line-ordered (blue), random (red), and cluster (green) alloys.

the possibility of synthesizing the newly predicted 2D material formed by a MoS_2 monolayer alloyed with O atoms. This plot of the formation energies shows that these different types of alloy follow the same trend. Although at 50/50 concentration, the hypothetical line-ordered is more energetically favorable. In addition, we found that the lowest energy configurations of the line-ordered competes with those that are already experimentally achieved (random and cluster) using other atoms, suggesting that all of them can be synthesized under the same conditions.

3.4. Structural properties of the O alloys in a MoS_2 monolayer

We now examine the effects of the O alloys on the lattice constants of a MoS_2 monolayer. We evaluate the lattice constants of the lowest energy configurations of the line-ordered, random and cluster obtained at each concentration shown in Fig. 8. We observe the three plots of the lattice constant to have the same trend, showing monotonously decrease due to the small atomic radii of the O atom compared to that of S atom. This trend is opposite to the previous result on MoS_2 monolayer alloyed with Te and Se atoms [15, 38] since they have large atomic radii compared to a S atom. For the three cases, the calculated values of the lattice constants of all configurations at every concentration ranges between those of the pristine MoS_2 (3.18 Å) and MoO_2 (2.81 Å) monolayers. Comparing the obtained values at each concentration for each shape of alloy, the magnitudes of the lattice constant are almost equal. This suggests that the area of the system does not really depend on the atomic arrangement but on the alloy concentration. We also in Fig. 8 plotted the lattice constants of these configurations obtained from the linear interpolations known as Vegard's law [60]. The reliability of this law has frequently been reported in the 3D [61, 62] and 2D TMD monolayer alloys [13, 14]. As seen in Fig. 8, we observe that the lattice constants of each type of alloy considered vary almost linearly, revealing that Vegard's law is being obeyed [63]. Usually, the fulfillment of this law indicates the existence of small lattice mismatch between the two pristine systems [60], in our case MoS_2 and MoO_2 monolayers.

To further analyze the intra-change in the structural properties at each concentration, the distribution of the first nearest bond lengths is measured.

We also compare the bond length deviation for each type of alloy considered in this study as shown in Fig. 9. We only present the bond lengths for the three different alloy shapes measured at 0.1 concentration, since the same observation is seen at higher concentrations. The measured Mo-S bond lengths for each alloy system are found to be constantly equal to that of a pristine MoS_2 monolayer, whereas a deviation from the pristine bond length value is noted for the Mo-O bonds. This deviation varies between 2.05 Å to 2.09 Å depending on the shape of alloy with a percentage difference of 1.93% (2.09 Å) for the line, 0.97-1.45% (2.07 Å, 2.08 Å) for the random and 0-0.49%

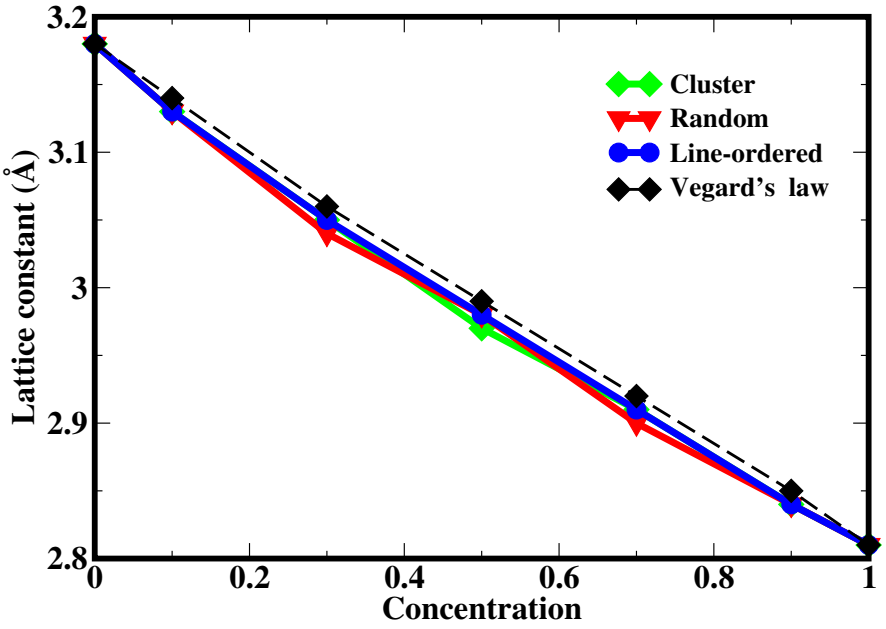

Figure 8: The variation in lattice constants for the lowest energy configuration at 0.1, 0.3, 0.5, 0.7 and 0.9 concentration, relative to the change in concentration. Blue, red and black solid lines connect the lattice constant at each concentration for the O line-ordered, random and cluster alloys respectively.

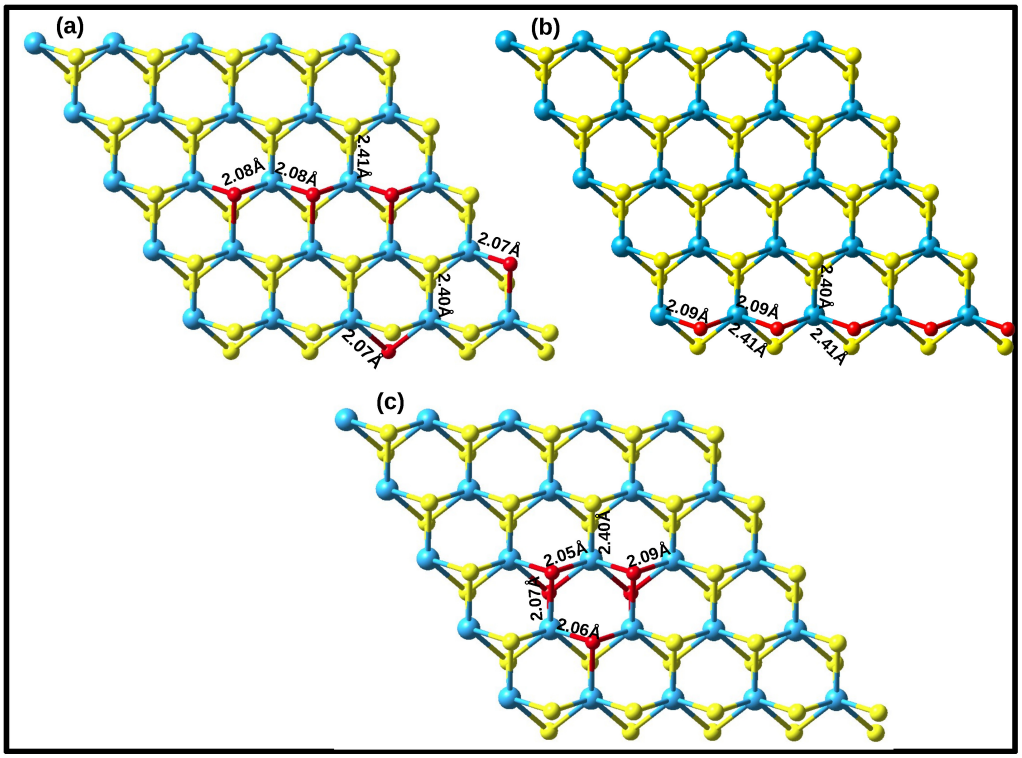

Figure 9: Top view of a hexagonal MoS_2 monolayer alloyed with 0.1 concentration of O atoms, showing the bond lengths (Mo-S) and (Mo-O) located at the various sites. The blue, red and yellow spheres indicate the Mo, O and S atoms respectively.

(2.05 Å, 2.06 Å) for the cluster. This small disparity in Mo-O bond length might be the cause of the slight differences in lattice constants for the three types of alloy studied. Since the bond length fluctuation of the various systems is not significant, the hexagonal symmetry from the top view of the host material is preserved after alloying.

Table 4: Calculated band gap values of the most stable configurations at every concentration for the O line-ordered, random and cluster configurations.

	Band gap(eV)					
	GGA			**HSE06**		
Concentration	Line	Random	Cluster	Line	Random	Cluster
0.1	1.50	1.50	1.60	2.00	2.12	2.15
0.3	1.39	1.43	1.53	1.97	2.00	2.10
0.5	1.18	1.37	1.45	1.82	1.90	2.02
0.7	1.12	1.19	1.29	1.63	1.75	1.93
0.9	1.02	1.12	1.03	1.58	1.60	1.66

The obtained band gap values are consistent with the values reported in ref. [64].

3.5. Electronic properties of the MoS_2 systems alloyed with O atoms

To examine the influence of the O atom alloys on the electronic properties of the MoS_2 monolayer, the total and partial density of states (TDOS and PDOS) at each concentration are plotted and shown in Fig.10. As seen in this figure, the alloyed systems retain the semiconducting features of the MoS_2 monolayer, although the band gap value decreases with the increase in O concentration. This suggests that the insertion of the O atoms in the MoS_2 monolayer can fine tunes the band gap of this system. To quantify this reduction, the band gaps of the most energetically stable configurations at each concentration for the O line-ordered, random and cluster alloys are measured and presented in Table 4. A common aspect of the electronic properties of the three shapes of alloys considered in this study is that the

band gap magnitudes of the various systems vary between the band gaps of the MoS_2 (1.65 eV for GGA and 2.17 eV for HSE06) and MoO_2 (0.98 eV for GGA and 1.48 eV for HSE06) monolayers. This range of the obtained band gap values is required for various applications such as solar cell, electronic applications, etc. Alternatively, the band gaps of the O random and cluster alloy configurations seem to be constantly higher than that of O line-ordered alloy. These observations suggest that the structural shape also have an influence on the band gap engineering in a MoS_2 monolayer alloyed with O atoms.

The PDOS shown in Fig.10 illustrates the origin of the reduction of the band gap. In this figure, we only present the PDOS of the O line-ordered alloys since the contribution of the orbitals at the band edges are the same for the three types of alloys. We found that the valence band maximum (VBM) is contributed by the d orbital of the Mo atoms and the p orbitals of the S and O atoms, while the conduction band minimum (CBM) is mainly dominated by the d orbitals of the Mo atoms. Therefore, the p orbital states from the O atoms introduced lie in the band edge and affect the hybridization of the Mo d orbital and S p orbital of the pristine MoS_2 monolayer, resulting in the band gap narrowing.

To have a deep understanding of the electronic interaction between the host material MoS_2 monolayer and the O atoms introduced, we also study the charge distribution at each site for each concentration as shown in Fig. 11. It can be seen that the VBM states of the O line-ordered alloy in a MoS_2 monolayer are localized around the Mo, S and O atoms, while the CBM states are concentrated around the Mo atoms only. These results are consistent with

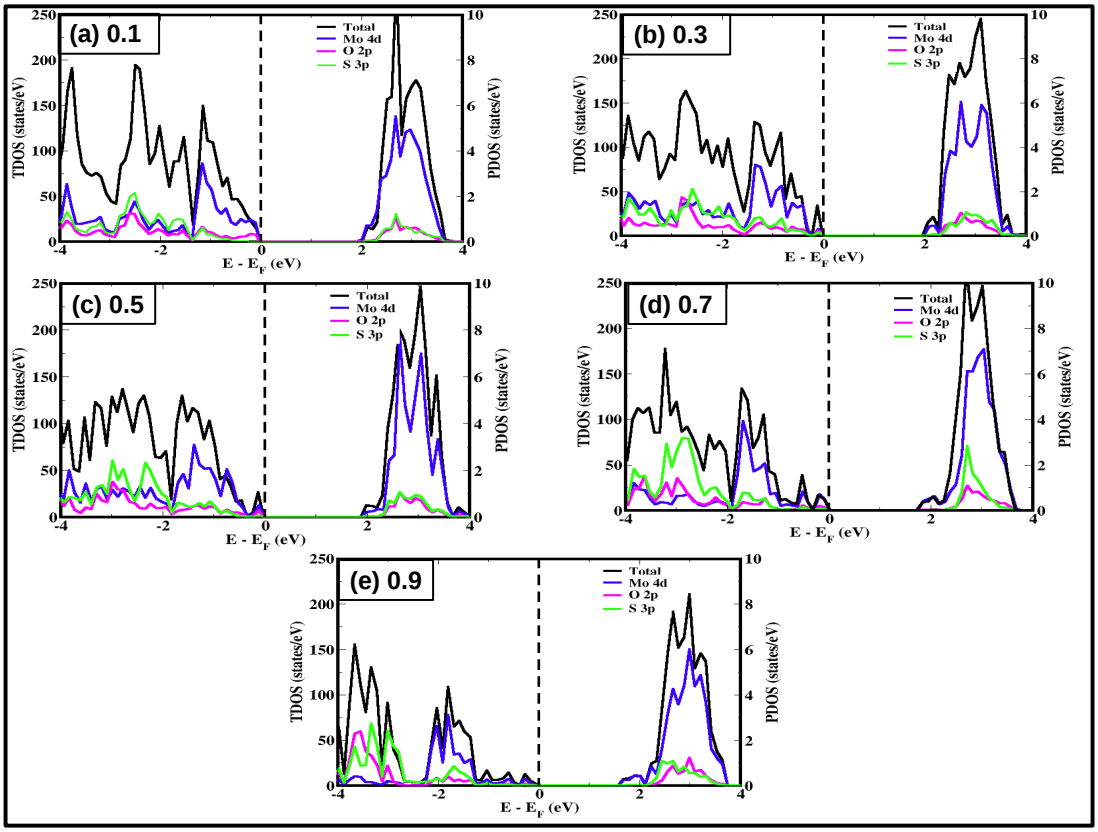

Figure 10: TDOS and PDOS of the lowest energy configuration at 0.1, 0.3, 0.5, 0.7 and 0.9 concentrations for the line-ordered alloy configurations obtained using HSE06 functional. The blue, magenta and green solid lines correspond to the Mo 4*d*, O 2*p* and S 3*p* orbitals respectively. The black solid line indicates the TDOS and the dashed vertical line represents the Fermi level

the PDOS observations described earlier (see Fig. 10). Furthermore, we also observe that the Mo atoms bonded with the O atoms along the O row have more charge compared to others.

Besides the transition from pristine MoS_2 to MoO_2 monolayers through alloying, stacking of these two different TMD monolayers is also expected

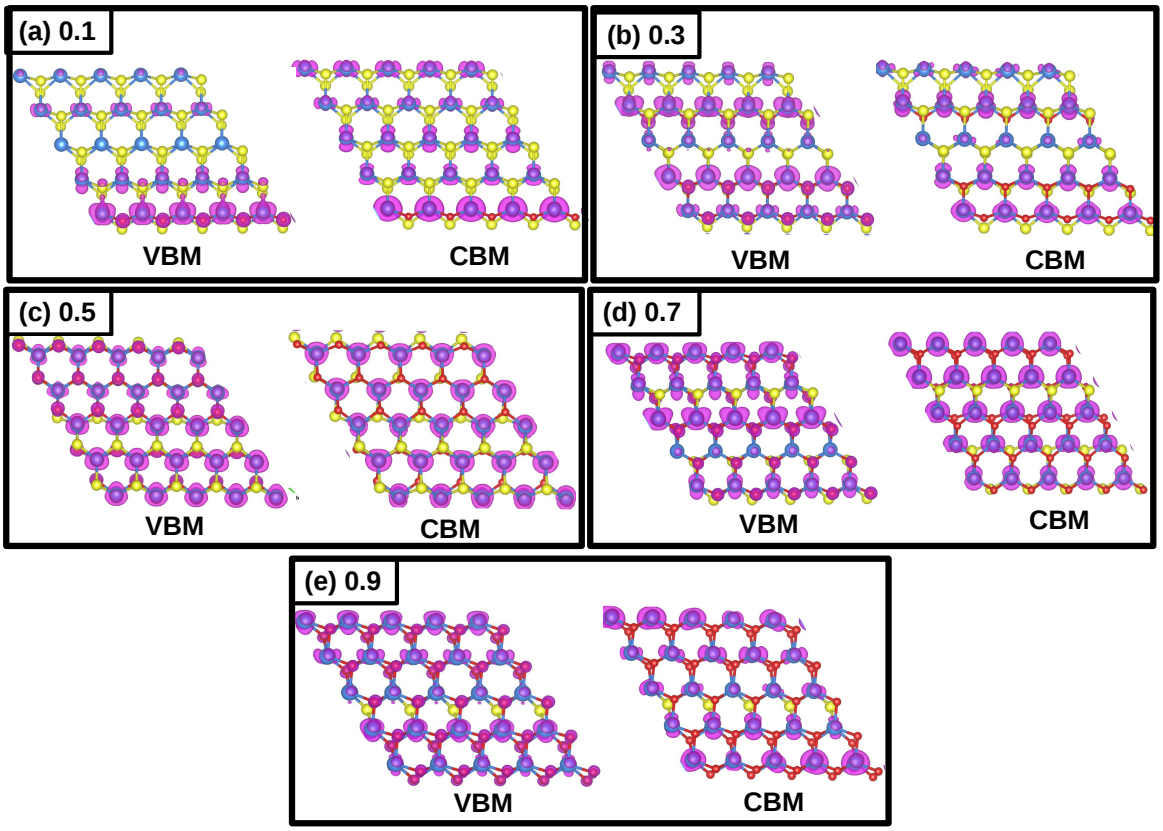

Figure 11: Partial charge density of the lowest energy configuration at each concentration. The blue, red and yellow spheres indicate the Mo, O and S atoms respectively.

to affect the electronic properties of these materials. In this study, the homobilayers (MoS_2/MoS_2 and MoO_2/MoO_2) and heterobilayer (MoO_2/MoS_2) are investigated for band gap engineering. The well known high-symmetry stacking orders such as AA, AA1 and AB are considered. (i) AA stacking is an eclipsed stacking with Mo atom facing Mo atom and S (or O) aligned with S (or O) atom of the subsequent layer. (ii) AA1 stacking is an eclipsed

stacking where Mo atom is on top of the S (or O) atom. (iii) Stacking type AB is a staggered stacking with S(or O) atom over Mo atom and Mo atom facing the center of the hexagon of the subsequent layer.

Table 5: The calculated formation energies $E_{form}(eV)$ and band gaps $E_{gap}(eV)$ of AA, AA1 and AB for homobilayers (MoS_2/MoS_2 and MoO_2/MoO_2) and heterobilayer (MoO_2/MoS_2).

Systems	properties	AA	AA1	AB
MoS_2/MoS_2	E_{form}	-0.31	-0.36	-0.34
	$E_{gap(GGA)}$	1.50	1.30	1.29
	$E_{gap(HSE)}$	2.10	1.95	1.90
MoO_2/MoO_2	E_{form}	1.09	1.08	1.15
	$E_{gap(GGA)}$	0.91	0.81	0.76
	$E_{gap(HSE)}$	1.47	1.45	1.30
MoO_2/MoS_2	E_{form}	0.40	0.37	1.3
	$E_{gap(GGA)}$	-	-	-
	$E_{gap(HSE)}$	-	-	-

The thermodynamic stability of these configurations is evaluated by calculating the formation energy using the following formula [65, 66]:

$$E_{form} = E_{stacking} - n_{MoS_2}E_{MoS_2} - n_{MoO_2}E_{MoO_2} \tag{4}$$

where $E_{stacking}$, E_{MoS_2} and E_{MoO_2} are the total energies of the stacked system, single layer of MoS_2 and MoO_2, respectively. n_{MoS_2} and n_{MoO_2} are the number of single layers of MoS_2 and MoO_2 present in the system. The energetics as well as the band gaps of the various configurations are summarized in Table. 5.

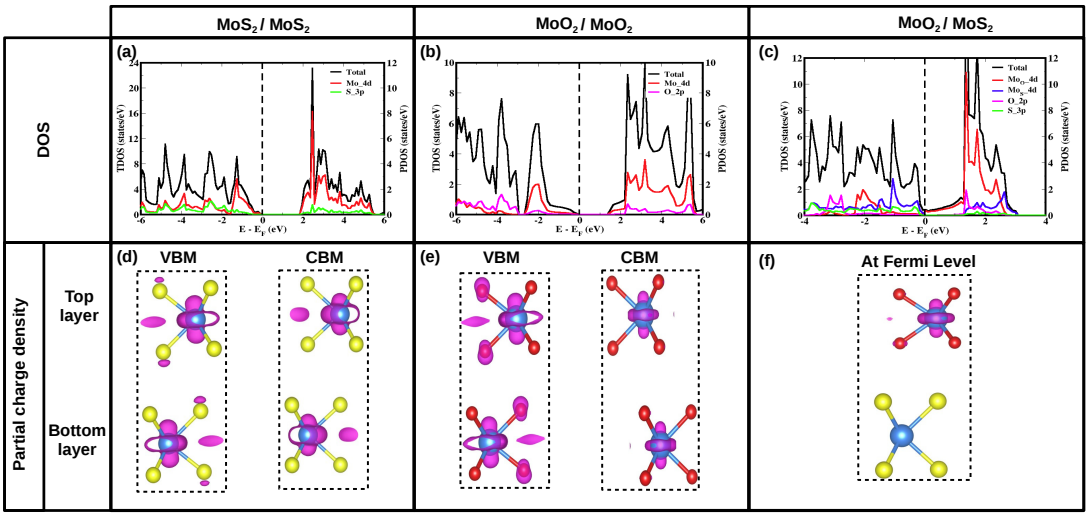

Figure 12: The calculated TDOS and PDOS of homobilayers (a) MoS_2/MoS_2, (b) MoO_2/MoO_2 and heterobilayer (c) MoO_2/MoS_2 for the most stable stacking (AA1). The dashed line represent the Fermi level. The calculated partial charge densities of homobilayers (d) MoS_2/MoS_2, (e) MoO_2/MoO_2 and heterobilayer (f) MoO_2/MoS_2.

For the homobilayer MoS_2/MoS_2 and MoO_2/MoO_2 systems, AA1 stacking is energetically most favorable. This is in good agreement with the previous theoretical work [65, 55]. Similarly, the stacking type AA1 has the lowest formation energy in the case of the heterobilayer MoO_2/MoS_2.

Regarding the electronic properties of these materials, the homobilayers MoS_2/MoS_2 and MoO_2/MoO_2 in different stacking are semiconductor materials with the reduced band gap values as compared to those of single layer counterparts. In both homobilayer cases, AA type presents the largest band gap value while AB type has the lowest value (see Table. 5). In order to understand the origin of the reduction in the band gap, the PDOS of the most energetically stable bilayers are depicted in Fig. 12. A downwards shift

of the CBM to the Fermi level is observed, and this is due to the presence of the 4*d* orbital of the Mo atom. This orbital states shift is mainly responsible for the reduction of the band gap. In the other hand, the VBM states are populated by the Mo 4*d* orbital and S 3*p* (O 2*p*) orbital. These distributions reconcile with the partial charge density analysis (see Fig. 12(d-e)). In the case of heterobilayer MoO_2/MoS_2, a metallic behavior is observed for all type of stacking orders. The PDOS reveal that the electronic states crossing the Fermi level arise from Mo 4*d* orbital of the MoO_2 layer (Fig. 12(c)). This is confirmed by the partial charge density distributions populated at the Mo atom of the MoO_2 layer (Fig. 12(f)).

4. Conclusion

In this paper, we performed a comparative study of all possible O line-ordered, cluster and random alloy configurations in a 5 $\times$ 5 supercell of MoS_2 monolayer for nanotechnological applications. An intensive comparative study on the thermodynamic stability, structural and electronic properties of these configurations have been considered. For each alloy shape, the most stable configuration at every concentration is identified and further characterized. Their noted relatively low formation energies suggest that these alloyed systems are thermodynamically stable and can easily be synthesized at low temperature using methods such as CVD technique or can easily be exfoliated from their bulk counterparts. The comparative study presented in this paper encourages the experimental synthesis of the line-ordered alloys since they are constantly energetically most stable at each concentration. Moreover, the effect of the O atoms greatly reduces the lat-

tice constant of the MoS_2 monolayer thereby obeying the Vegard's law. Most importantly, alloying with the O atoms fine tunes the band gap of the MoS_2 monolayer. The range of the obtained band gap values (2.17 eV (MoS_2) - 0.98 eV (MoO_2)) satisfies the requirement of nanoelectronic and solar cell applications. Creation of stacking of MoS_2 with MoO_2 gives metallic character, with Mo $4d$ orbital crossing the Fermi level. In conclusion, the O atom concentration and the atomic arrangement greatly affect the electronic structures of the MoS_2 monolayer, and the noted band gap variation can be beneficial for electronic device design.

Acknowledgment

The authors would like to acknowledge the University of Pretoria for computational resources and financial support. NC would also like to thank the National Institute of Theoretical Physics for financial support.

References

[1] B. Radisavljevic, A. Radenovic, J. Brivio, i. V. Giacometti, A. Kis, Nat. Nanotechnol 6 (3) (2011) 147–150.

[2] C. Lee, X. Wei, J. W. Kysar, J. Hone, science 321 (5887) (2008) 385–388.

[3] A. Kuc, T. Heine, A. Kis, MRS Bulletin 40 (7) (2015) 577–584.

[4] Y. Kubota, K. Watanabe, O. Tsuda, T. Taniguchi, Science 317 (5840) (2007) 932–934.

[5] A. K. Geim, K. S. Novoselov, Nat. Mater 6 (3) (2007) 183–191.

[6] J. C. Meyer, A. Chuvilin, G. Algara-Siller, J. Biskupek, U. Kaiser, Nano Lett 9 (7) (2009) 2683–2689.

[7] K. F. Mak, C. Lee, J. Hone, J. Shan, T. F. Heinz, Phys. Rev. Lett 105 (13) (2010) 136805.

[8] L. Xie, Nanoscale 7 (44) (2015) 18392–18401.

[9] C. Ataca, H. Sahin, S. Ciraci, J. Phys. Chem. C 116 (16) (2012) 8983–8999.

[10] F. A. Rasmussen, K. S. Thygesen, J. Phys. Chem. C 119 (23) (2015) 13169–13183.

[11] Y. Zhou, C. Geng, Nanotechnology 28 (10) (2017) 105402.

[12] H.-P. Komsa, A. V. Krasheninnikov, J. Phys. Chem. Lett 3 (23) (2012) 3652–3656.

[13] J. Kang, S. Tongay, J. Li, J. Wu, J. Appl. Phys 113 (14) (2013) 143703.

[14] N. Andriambelaza, R. Mapasha, N. Chetty, J. Phys. Condens. Matter 29 (32) (2017) 325504.

[15] B. Rajbanshi, S. Sarkar, P. Sarkar, Phys. Chem. Chem. Phys 17 (39) (2015) 26166–26174.

[16] H.-P. Komsa, A. V. Krasheninnikov, Phys. Rev. B 91 (12) (2015) 125304.

[17] K. Santosh, R. C. Longo, R. Addou, R. M. Wallace, K. Cho, Nanotechnology 25 (37) (2014) 375703.

[18] S. Haldar, H. Vovusha, M. K. Yadav, O. Eriksson, B. Sanyal, Phys. Rev. B 92 (23) (2015) 235408.

[19] C. González, B. Biel, Y. J. Dappe, Nanotechnology 27 (10) (2016) 105702.

[20] S.-C. Lu, J.-P. Leburton, Nanoscale Res. Lett 9 (1) (2014) 676.

[21] K. Dolui, I. Rungger, C. D. Pemmaraju, S. Sanvito, Phys. Rev. B 88 (2013) 075420.

[22] A. V. Krivosheeva, V. L. Shaposhnikov, V. E. Borisenko, J.-L. Lazzari, C. Waileong, J. Gusakova, B. K. Tay, J. Semicond. 36 (12) (2015) 122002.

[23] J. Suh, T.-E. Park, D.-Y. Lin, D. Fu, J. Park, H. J. Jung, Y. Chen, C. Ko, C. Jang, Y. Sun, et al., Nano letters 14 (12) (2014) 6976–6982.

[24] Y.-C. Lin, D. O. Dumcenco, H.-P. Komsa, Y. Niimi, A. V. Krasheninnikov, Y.-S. Huang, K. Suenaga, Adv. Mater. 26 (18) (2014) 2857–2861.

[25] Q. Yue, J. Kang, Z. Shao, X. Zhang, S. Chang, G. Wang, S. Qin, J. Li, Phys. Lett A 376 (12-13) (2012) 1166–1170.

[26] P. Lu, X. Wu, W. Guo, X. C. Zeng, Phys. Chem. Chem. Phys. 14 (37) (2012) 13035–13040.

[27] E. Scalise, M. Houssa, G. Pourtois, V. Afanasev, A. Stesmans, Nano Research 5 (1) (2012) 43–48.

[28] K. He, C. Poole, K. F. Mak, J. Shan, Nano letters 13 (6) (2013) 2931–2936.

[29] P. Johari, V. B. Shenoy, ACS nano 6 (6) (2012) 5449–5456.

[30] D. Dumcenco, K. Chen, Y. Wang, Y. Huang, K. Tiong, J. Alloys Compd 506 (2) (2010) 940–943.

[31] Y. Chen, J. Xi, D. O. Dumcenco, Z. Liu, K. Suenaga, D. Wang, Z. Shuai, Y.-S. Huang, L. Xie, Acs Nano 7 (5) (2013) 4610–4616.

[32] T. L. Tan, M.-F. Ng, G. Eda, J. Phys. Chem. C 120 (5) (2016) 2501–2508.

[33] X.-L. Wei, H. Zhang, G.-C. Guo, X.-B. Li, W.-M. Lau, L.-M. Liu, J. Mater. Chem. A 2 (7) (2014) 2101–2109.

[34] P. M. Larsen, A. R. Kalidindi, S. Schmidt, C. A. Schuh, Acta Mater. 139 (2017) 254–260.

[35] L.-Y. Gan, Q. Zhang, Y.-J. Zhao, Y. Cheng, U. Schwingenschlögl, Scientific reports 4 (2014) 6691.

[36] Q. Feng, N. Mao, J. Wu, H. Xu, C. Wang, J. Zhang, L. Xie, ACS nano 9 (7) (2015) 7450–7455.

[37] Q. Feng, Y. Zhu, J. Hong, M. Zhang, W. Duan, N. Mao, J. Wu, H. Xu, F. Dong, F. Lin, et al., Adv. Mater 26 (17) (2014) 2648–2653.

[38] N. Andriambelaza, R. Mapasha, N. Chetty, Physica B: Condens. Matter 535 (2018) 162 – 166.

[39] G. Kresse, J. Furthmüller, Phys. Rev. B 54 (16) (1996) 11169.

[40] J. P. Perdew, K. Burke, M. Ernzerhof, Phys. Rev. Lett 77 (18) (1996) 3865.

[41] Á. Morales-García, R. Valero, F. Illas, J. Phys. Chem. C 121 (34) (2017) 18862–18866.

[42] J. Heyd, G. E. Scuseria, M. Ernzerhof, J. Chem. Phys. 118 (18) (2003) 8207–8215.

[43] Y. Zhong, A. Luo, J. Nie, J. O. Sofo, Z.-K. Liu, in: Essential Readings in Magnesium Technology, Springer, 2016, pp. 427–432.

[44] C. Jiang, Y. Du, J. Appl. Phys 109 (2) (2011) 023504.

[45] U. K. Sen, P. Johari, S. Basu, C. Nayak, S. Mitra, Nanoscale 6 (17) (2014) 10243–10254.

[46] J. Su, N. Li, Y. Zhang, L. Feng, Z. Liu, AIP Advances 5 (7) (2015) 077182.

[47] Y. Li, Y.-L. Li, C. M. Araujo, W. Luo, R. Ahuja, Catal. Sci. Technol 3 (9) (2013) 2214–2220.

[48] P. Young, J. Phys. D Appl. Phys. 1 (7) (1968) 936.

[49] A. Ramirez-Torres, D. Le, T. S. Rahman, in: IOP Conf. Ser. Mater. Sci. Eng., Vol. 76, IOP Publishing, 2015, p. 012011.

[50] H. Wan, L. Xu, W.-Q. Huang, J.-H. Zhou, C.-N. He, X. Li, G.-F. Huang, P. Peng, Z.-G. Zhou, RSC Adv. 5 (11) (2015) 7944–7952.

[51] C. Ataca, S. Ciraci, J. Phys. Chem. C 115 (27) (2011) 13303–13311.

[52] D. Wang, L.-M. Liu, S.-J. Zhao, Z.-Y. Hu, H. Liu, J. Phys. Chem. C 120 (9) (2016) 4779–4788.

[53] A. Kumar, P. Ahluwalia, Mater. Chem. Phys. 135 (2-3) (2012) 755–761.

[54] Y. Ji, M. Yang, H. Lin, T. Hou, L. Wang, Y. Li, S.-T. Lee, J. Phys. Chem. C 122 (5) (2018) 3123–3129.

[55] Z. Fan, Z. Wei-Bing, T. Bi-Yu, Chin. Phys. B 24 (9) (2015) 097103.

[56] Y. Jing, X. Tan, Z. Zhou, P. Shen, J. Mater. Chem. A 2 (40) (2014) 16892–16897.

[57] J. Zhang, S. Jia, I. Kholmanov, L. Dong, D. Er, W. Chen, H. Guo, Z. Jin, V. B. Shenoy, L. Shi, et al., ACS nano 11 (8) (2017) 8192–8198.

[58] A. Zunger, S.-H. Wei, L. Ferreira, J. E. Bernard, Phys. Rev. Lett 65 (3) (1990) 353.

[59] Y. Huang, X. Chen, D. Zhou, H. Liu, C. Wang, J. Du, L. Ning, S. Wang, J. Phys. Chem. C 120 (10) (2016) 5839–5847.

[60] K. Jacob, S. Raj, L. Rannesh, Int. J. of Mater. Res 98 (9) (2007) 776–779.

[61] Y. Mao, X. Liang, G. Zhao, T. Song, in: J. Phys. Conf. Se, Vol. 490, IOP Publishing, 2014, p. 012172.

[62] H. M. Foronda, B. Mazumder, E. C. Young, M. A. Laurent, Y. Li, S. P. DenBaars, J. S. Speck, J. Cryst. Growth 475 (2017) 127–135.

[63] A. R. Denton, N. W. Ashcroft, Phys. Rev. A 43 (6) (1991) 3161.

[64] S. KC, R. C. Longo, R. M. Wallace, K. Cho, J. Appl. Phys 117 (13) (2015) 135301.

[65] T. Peng, G. Huai-Hong, Y. Teng, Z. Zhi-Dong, Chin. Phys. B 23 (10) (2014) 106801.

[66] W. Wei, Y. Dai, B. Huang, Phys. Chem. Chem. Phys. 19 (1) (2016) 663–672.